Yang *et al. BMC Medical Informatics and Decision Making* (2025) 25:185
https://doi.org/10.1186/s12911-025-03009-4

BMC Medical Informatics and Decision Making

RESEARCH

Open Access

Application of artificial intelligence medical imaging aided diagnosis system in the diagnosis of pulmonary nodules

Ya Yang[1], Pan Wang[1], Chengzhou Yu[2], Jing Zhu[1] and Jinping Sheng[1*]

Abstract
The application of artificial intelligence (AI) technology has realized the transformation of people's production and lifestyle, and also promoted the rapid development of the medical field. At present, the application of intelligence in the medical field is increasing. Using its advanced methods and technologies of AI, this paper aims to realize the integration of medical imaging-aided diagnosis system and AI, which is helpful to analyze and solve the loopholes and errors of traditional artificial diagnosis in the diagnosis of pulmonary nodules. Drawing on the principles and rules of image segmentation methods, the construction and optimization of a medical image-aided diagnosis system is carried out to realize the precision of the diagnosis system in the diagnosis of pulmonary nodules. In the diagnosis of pulmonary nodules carried out by traditional artificial and medical imaging-assisted diagnosis systems, 231 nodules with pathology or no change in follow-up for more than two years were also tested in 200 cases. The results showed that the AI software detected a total of 881 true nodules with a sensitivity of 99.10% (881/889). The radiologists detected 385 true nodules with a sensitivity of 43.31% (385/889). The sensitivity of AI software in detecting non-calcified nodules was significantly higher than that of radiologists (99.01% vs 43.30%, P < 0.001), and the difference was statistically significant.

Keywords Medical imaging assisted diagnosis system, AI, Image segmentation, Pulmonary nodule diagnosis

Introduction

With the rapid development of modern science and technology, AI technology continues to involve various fields of work and life. Healthcare is an important area of rapid development of AI applications. At present, the combination of AI technology and medical imaging methods has become a research hotspot in this field, and related research results have shown explosive growth. The AI-assisted diagnosis system provides an intelligent auxiliary diagnosis system for medical images based on deep learning, which deeply integrates the workflow of human radiologists and provides intelligent auxiliary diagnosis information in the process of doctor reading. This helps physicians complete imaging diagnosis, reduces misdiagnosis, misdiagnosis and missed diagnosis, and improves work efficiency. Lung cancer is one of the malignant tumors that pose the greatest threat to human health worldwide, and its morbidity and mortality ranks first among all malignant tumors. Thin-slice CT technology is helpful for the early detection of lung cancer, but thin-slice CT increases the incidence of lung cancer. The

*Correspondence:
Jinping Sheng
zetreo0768@163.com
[1]Department of Radiology, Chinese People's Liberation Army The General Hospital of Western Theater Command, No. 270, Tianhui Road, Rongdu Avenue, Jinniu District, Chengdu, Sichuan 610083, China
[2]Chinese People's Liberation Army Marine Corps Hospital, Chaozhou, Guangdong 521000, China

amount of X-rays read by CT images and image doctors can lead to missed and misdiagnosed lung nodules.

Several companies have developed AI CT screening platforms. The value and advantages of the AI screening system in clinical application, the most intuitive is the fast reading speed of the AI screening system. The work that doctors need a few minutes to ten minutes to complete, the AI screening system can solve in only about 3 seconds. The second is that the AI-aided diagnosis system has no fatigue. With the increase of working hours, the mental state of radiologists gradually decreased from good to fatigue. Doctors' diagnosis and response are poor after fatigue, while AI does not. It has high diagnostic efficiency and can also reduce the missed diagnosis rate of small pulmonary nodules to a certain extent. In addition to screening pulmonary nodules, AI can observe subtle changes in lesions better than human vision, and some quantitative parameters are conducive to the qualitative diagnosis of lesions.

The application of AI technology is an important process for the medical field. It is a very innovative project in the diagnosis of the pulmonary nodules of medical images. Many scholars have conducted research on this. Among them, Zheng G proposed an integrated classification method based on the INCEPTION module to diagnose lung nodule with different nodule signs[1]. Zhang S used the classic LENET-5 model to classify the lung nodules of the chest CT image [2]. The purpose of Zhang N was to investigate the value of CT texture analysis in the differential diagnosis of benign and malignant solitary pulmonary nodules (SPNs). The method he proposed performed CT scans on 97 SPN patients (54 in the malignant group and 43 in the benign group) to measure the CT value and maximum diameter of the nodules [3]. Vayntrub Y evaluated the lung nodule through PET to verify the Herder model [4]. Wang Y found that CAD based on deep learning is the mainstream of the current research [5]. Although these studies have promoted the application of AI in the medical field to a certain extent, they are still in the theoretical stage in today's environment, and have little effect in practice.

In order to promote more accurate and rationalized diagnosis of pulmonary nodules, traditional diagnostic methods need to be improved. Therefore, some scholars propose to use medical imaging-assisted diagnosis systems to accurately diagnose pulmonary nodules. Among them, Singh S provided a computer diagnostic system that can automatically generate radiological reports from medical images to reduce loads [6]. Ha W introduced an automated breast tumor diagnosis system [7]. Saygili A proposed a new three-stage (preprocessing, segmentation, and classification) method [8]. The study of Barinov L proved the significant accuracy difference between the two diagnostic systems [9]. Loku L's study investigated peer-reviewed research to understand the current state of the clinical application of empirically-based evidence in the diagnosis and treatment of autism spectrum disorder (ASD). Different sensing techniques for ASD have also been investigated and investigated [10]. Although the above studies mention advances in the diagnosis of various formal wear using medical imaging systems, they all only address a single aspect of medical imaging applications, resulting in a lack of comprehensive understanding.

In this paper, an AI-based medical imaging diagnosis assistant system is used for the diagnosis of pulmonary nodules, and the clinical application of the AI assistant diagnosis system for pulmonary nodules is carried out by using the subjective image quality evaluation method. In the same test for 200 patients with a total of 231 nodules with pathology or no change after two years of follow-up. The results showed that 881 true nodules were detected using AI software, and the sensitivity was 99.10 % (881/889). The radiologist detected 385 true nodules with a sensitivity of 43.31 % (385/889). AI software detects the sensitivity of uninterrupted nodules than that of radiologists (99.01 % vs 43.30 %, $P<0.001$), and the difference is statistically important [11]. AI software can detect the sensitivity of uninterrupted nodules with diameter < 5 mm ($P=0.000$), and the sensitivity of the diameter between 5–10 mm is more sensitive than the radiologist, and the difference is statistically

The innovation of this paper is to describe the application of the medical image assistance system based on AI technology in the medical field, which has significant advantages in all aspects. Not only can the radiation dose of chest CT scans be further reduced, more nodules can be detected and marked, but lung nodules can be located, characterized, and even predicted tumor growth, but also can predict the pathological grading of malignant lung nodules, the occurrence of metastasis and the clinical prognosis of tumors [12]. At present, a large number of studies have shown that AI can effectively reduce the workload of radiologists, liberate the labor force of doctors, and reduce the rate of missed diagnosis of pulmonary nodules by doctors.

Medical imaging diagnosis assistance system in the diagnosis of pulmonary tuberculosis

Overall scheme design

The AI aided diagnosis system for pulmonary nodules is divided into two parts: cloud server design and user interface design, and file transmission and instruction interaction are carried out through the designed transmission module. Its overall structure is shown in Fig. 1.

It can be seen from Fig. 1 that the client architecture is composed of CT display, file selection, interface

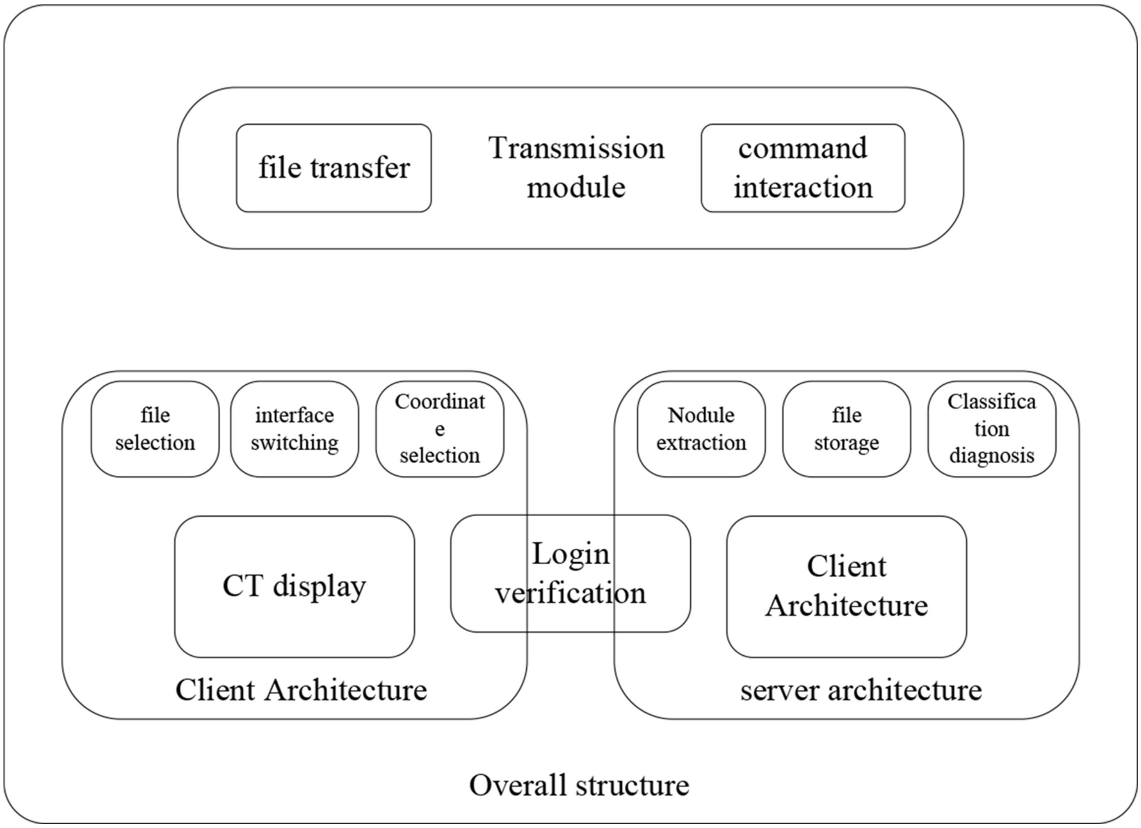

Fig. 1 Overall system architecture

switching and coordinate selection, and its functions are as follows:

(1) Login verification

Creating a user login verification interface, and designing three login prompt boxes, which correspond to the cases where the user name does not exist, and the user's name and password match successfully. After the first two cases are prompted, the interface remains as it is and can be re-entered. If the login is successful, the interface can be jumped.

(2) File operation

The operation function of the file is mainly to select the CT image file to be processed and upload it to the cloud server through the file transfer function in the transmission module. During the system operation, the intermediate files and result data generated by the server operation are sent back to the client, and the returned result information is displayed in the interface in a visual form [13].

(3) CT image display

An important function of the system is to display CT images. Considering that the CT images used are in the DICOM format, after selecting the folder where the CT images to be processed are located through the file operation function, use the Visual Toolkit to import the DICOM files. The VTK window is embedded in the interface for display, and operations such as zooming in, zooming out, and flipping the CT image are realized at the same time. The interface adds a slider and edits the algorithm, which can adjust the brightness and contrast of the CT image by adjusting the slider.

(4) Instruction interaction

The interaction between the client and the server can execute Linux commands on the remote server through the command interaction function of the transmission module to perform operations such as nodule extraction, classification diagnosis, and result storage in the cloud server.

(5) Determination of location information of pulmonary nodules

It clicks the CT image displayed in the interface window, resets mouse events and drawing events, determines the click position, and calculates the coordinates of the lung nodule by combining the interface size and the pixel value of the CT image. At the same time, through the nodule size extraction box in the interface, this study selects the extraction box suitable for the nodule size. After the selection is completed, the results are uploaded to the cloud server through the transmission module to provide location information for the extraction of lung nodule volume data.

Cloud server-side functions

(1) MySQL database

A MySQL database is established on the cloud server side, and the database is designed to manage user data. It supports the query and verification function of user login name and password, and hierarchically stores information such as user login time, uploaded data, and calculation results for users to retrieve and query at any time.

(2) Extraction and storage of lung nodule volume data

The file uploaded by the client is saved, and the file is processed to obtain lung CT image data and lung nodule location information. The lung nodule area to be extracted is obtained by calculation and feature extraction is performed on the area, and the extracted data is saved through the assigned path and level, so that the extracted nodule area can be classified and diagnosed next.

(3) Classification diagnosis

According to the idea of deep residual network model, dense connection network model and multi-resolution processing, a multi-resolution 3D dual-path network model is built on the cloud server side to classify and diagnose the extracted lung nodule volume data. And the diagnostic result data is saved through the assigned path and level for the user to call. The overall flow chart of the AI-aided diagnosis system for pulmonary nodules is shown in Fig. 2.

As can be seen from Fig. 2, the AI aided diagnosis system for pulmonary nodules is written in Python language, and the deep learning network for diagnosing pulmonary nodules is built on the TensorFlow platform [14].

The core of the computer-aided diagnosis algorithm design lies in the construction of a multi-resolution 3D dual-path network model, which combines the ideas of

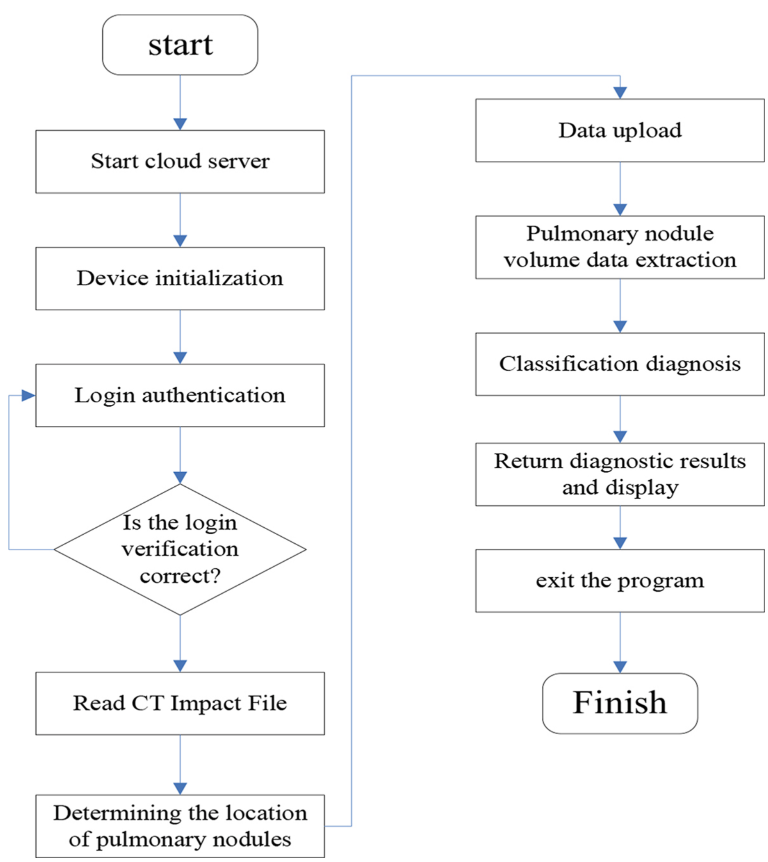

Fig. 2 Schematic diagram of the overall flow of the artificial aided diagnosis system for pulmonary nodules

deep ResNet and DenseNet. Specifically, the algorithm first extracts the volume data of lung nodules through multi-resolution processing technology, and then uses a dual-path network for feature extraction and classification diagnosis. The network contains multiple paths, each of which processes data of different scales and resolutions, thereby enhancing the diversity of feature extraction. By training the deep learning model on the TensorFlow platform, the system is able to identify various features of lung nodules and output corresponding diagnostic results. These results are saved and available for users to call through specified paths and levels to ensure convenient access and management of data.

During the training and verification process of the algorithm, a large amount of labeled lung nodule image data needs to be collected as training sets and verification sets. During training, the back propagation algorithm in deep learning is used to optimize the model, and the classification accuracy is improved by continuously adjusting the weight parameters in the network. During the training process, the cross-validation method is used to evaluate the performance of the model to ensure its generalization ability on different data sets. During the verification process, by comparing the model's prediction results on the verification set with the actual annotations, the model's structure and parameters are further optimized, and finally a model with high diagnostic accuracy is obtained. This process is carried out in Python language and TensorFlow framework, and combined with PyQt5 development framework to provide a user-friendly interactive interface.

Design of the interaction function between the client and the cloud server

(1) SSH protocol for server connection design

The secure shell protocol uses the DH algorithm to realize key exchange, and performs authentication based on RSADSA to ensure login security. The protocol framework of SSH is shown in Fig. 3.

SSH adopts a Client-Server structure. Paramiko is a Python library that encapsulates the SSHv2 protocol. Using the Paramiko library, the SSH protocol is used in the Python language to control remote computers. The aramiko library has two important components: SSHClient and SFTPClient. SFTPClient has similar functions to sftp commands and is used to complete remote file operations. SSHClient is a package of connections, and its function is similar to the Linux ssh command. It packaged the transport, channel and SFTPClient creation method. The channel is a secure SSH transmission path [15, 16]. Transport encrypts the call and then transmits it. It is generally used to create a remote client and send remote commands on the client. Session is the process that keeps the Client and Server talking.

(2) Realization of the interaction function between files and instructions

By establishing SSH connection between the client and the cloud server, the file operation uses the sftp class encapsulated in the paramiko module, which can be used for file upload, file download, directory creation and other operations. First it selects the QPushButton

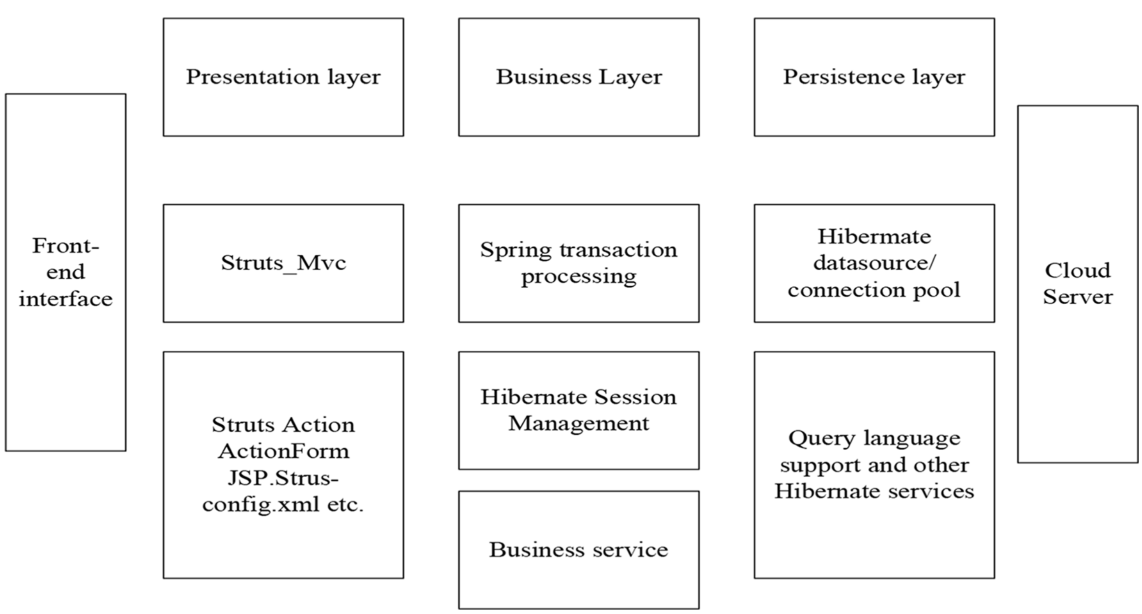

Fig. 3 SSH protocol framework

button in the interface instantiation file. The button signal emission method is set to clicked, that is, the signal is sent when the left mouse button is clicked on the button. The button event is associated with the function self.xuanzeO, and then the event implementation process is written in the self.xuanze() function. The FileDialog class can be used to select paths to files and folders, and QFileDialog displays the filename with the selected suffix while displaying the file list. Since the CT image files to be uploaded are multiple DICOM format files saved in the folder, the getExistingDirectory() function of QFileDialog is used here to select the existing files. The value of the selected folder path is returned to self.path, and the for statement is used to poll the file name dicom_name in the folder. The upload function is set to sftp.put. The folder path selfpath and the file name dicom.name can form the local file path localpath. At the same time, the path self.cloud path, the path self.cloud_path and the local file name dicom of the uploaded file on the cloud server side are newly created. _name can form the storage path on the cloud server side. The folder path self.cloud_path of each file is the same to ensure that it is sent to the same folder on the server side. The upload process is shown in Fig. 4.

After the above process, the related files such as lung CT images to be processed have been transmitted from the client to the cloud server, and then Linux commands can be sent from the client to the cloud server for data processing and other operations. Directives execute remote commands on the server side. This command creates a new channel and executes the instruction whose input stream and output stream are standard input, output, error object return form. *command* encapsulates the instruction to be executed, and timeout sets the timeout time for command execution [17, 18].

Subjective image quality evaluation method

The subjective evaluation method of the image is that many experienced medical workers observe the result image of the enhanced processing in this paper and make empirical comments. It is mainly based on the professional theoretical knowledge and medical work experience of medical workers to evaluate and score the quality of images. Because no reference object is involved, this method is also called absolute subjective evaluation. The relative subjective evaluation is based on the comparison of human eye observation with relatively undistorted images of better quality. Differential subjective score method calculation Equation:

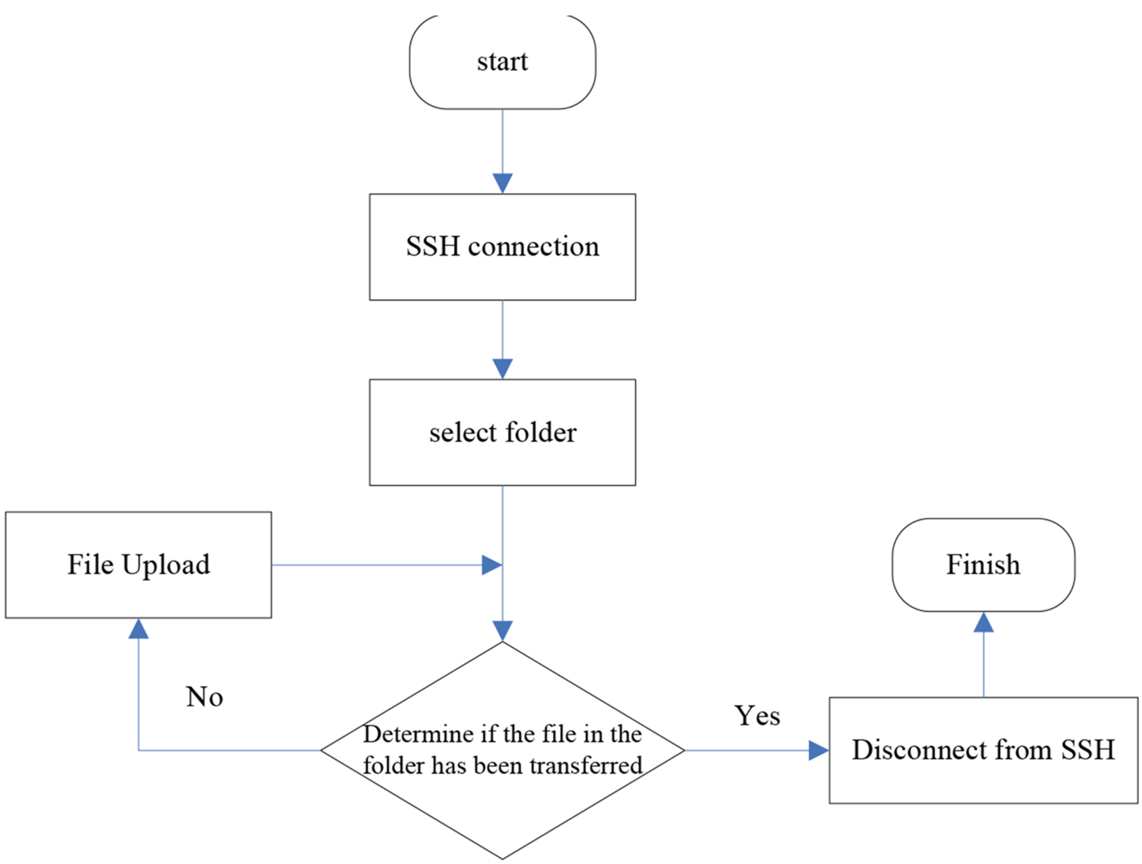

Fig. 4 File upload process

$$d_{i,j} = MOS_{origial} - MOS_{disorted} \tag{1}$$

$$d'_{i,j} = \frac{d_{i,j} - \min(d_{i,j})}{\max(d_{i,j}) - \min(d_{i,j})} \tag{2}$$

The MOS value here refers to a subjective score (one to five, ranging from worst, poor, average, better to best), $d_{i,j}$ refers to the MOS difference between the reference image and the evaluated image, usually the MOS of the reference image The value can be four or five, with $d_{i,j}$ being the average.

Objective image quality evaluation method

Because in the actual image quality evaluation, subjective evaluation is not accurate and scientific. It will be limited by the self-generated experience of medical work, lack of theoretical knowledge, and emotional factors, which make the image evaluation inaccurate. Therefore, the evaluation method without reference is adopted in this paper, and the evaluation is performed by calculating the relevant parameter values of the gray level co-occurrence matrix. The specific parameters are as follows:

(1) Energy: The Equation is shown in Equation 3:

$$ASM = \sum\nolimits_{i=0}^{L-1} \sum\nolimits_{j=0}^{L-1} P_d^2(i,j) \tag{3}$$

(2) Contrast: The Equation is shown in Equation 4:

$$CON = \sum\nolimits_{N=0}^{L-1} n^2 \left\{ \sum\nolimits_{j=0}^{L-1} \widehat{P}_d(i,j) \right\} \tag{4}$$

(3) Correlation: The Equation is shown in Equation 5:

$$COR = \frac{\sum\nolimits_{i=0}^{L-1} \sum\nolimits_{j=0}^{L-1} ij\hat{P}_d(i,j) - \mu_1\mu_2}{\sigma_1^2\sigma_2^2} \tag{5}$$

In the Equation, μ_1, μ_2, σ_1 and σ_2 are respectively the following Equations:

$$\mu_1 = \sum\nolimits_{i=0}^{L-1} i \sum\nolimits_{i=0}^{L-1} \hat{P}(i,j) \tag{6}$$

$$\mu_2 = \sum\nolimits_{i=0}^{L-1} i \sum\nolimits_{j=0}^{L-1} \widehat{P}_d(i,j) \tag{7}$$

$$\sigma_1^2 = \sum\nolimits_{i=0}^{L=1} (i-\mu_1)^2 \sum\nolimits_{j=0}^{L-1} \widehat{P}d(i,j) \tag{8}$$

$$\sigma_2^2 = \sum\nolimits_{i=0}^{L=1} (i-\mu_2)^2 \sum\nolimits_{j=0}^{L-1} \widehat{P}d(i,j) \tag{9}$$

(4) Entropy: The Equation is shown in Equation 10:

$$H = \sum\nolimits_{i=0}^{L-1} \sum\nolimits_{j=0}^{L-1} \widehat{P}_d(i,j) \log \widehat{P}_d(i,j) \tag{10}$$

(5) The Equation is shown in Equation 11:

$$l(X,Y) = \frac{2\mu_X + \mu_Y + C_1}{\mu^2{}_X + \mu^2{}_Y + C_1} \tag{11}$$

$$c(X,Y) = \frac{2\sigma_X\sigma_Y + C_2}{\sigma_X + \sigma_Y + C_2} \tag{12}$$

$$S(X,Y) = \frac{\sigma XY + C_3}{\sigma_X^2\sigma_Y^2 + C_2} \tag{13}$$

Among them: μ_x, μ_y, ${\sigma_X}^2$, ${\sigma_Y}^2$, and σ_{XY} represent the mean value and the standard deviation of x and y in the x and y directions of the evaluated image, respectively [19]. Covariance: C_1, C_2, C_3 is a constant, L is the dynamic range of the pixel gray value of the evaluation image. For eight-bit grayscale images, L = 255; for sixteen-bit grayscale images, L = 65535. The Equation for calculating the structural similarity of an image is:

$$SSIM(X,Y) = [l(X,Y)]^a * [c(X,Y)]^\beta * [S(X,Y)]^\gamma \tag{14}$$

Let

$$a = \beta = \gamma = 1 \tag{15}$$

By improving the algorithm based on the improvement research and referring to the relevant characteristics of the human visual imaging system, the definition evaluation index of the non-reference image is designed. The Equation for calculating the structural clarity is as follows:

$$NRSS = 1 - \frac{1}{N}\sum\nolimits_{i=1}^{N} SSIM(X_i, Y_i) \tag{16}$$

Improved OTSU lung parenchyma segmentation

The OTSU algorithm is an algorithm that determines the optimal segmentation threshold through an exhaustive search, and it has become a relatively mature lung parenchyma segmentation algorithm. Its process is shown in Fig. 5:

The specific algorithm principle is: In this paper, the medical image in DICOM format provided by a city people's hospital is used, and the gray level is 16 bits, so L is 65536. The number of pixels with a gray value of i is n, then the number of pixels in the image is the sum of all gray values:

$$N = \sum\nolimits_{i=0}^{L-1} n_i \tag{17}$$

Probability of occurrence of gray level: It can be defined as the number of pixels of this gray value in the total number of pixels.

$$p_i = \frac{n_i}{N}, \qquad i = 0, 1, 2, \ldots, L-1 \tag{18}$$

Then look for a valley threshold value t through the histogram of the image, and use this threshold value t to divide the image into two parts: namely Co = (0,1…). C1 = (t + 1,t + 2, t + 3, …… L-1), the probabilities of these two parts are:

$$\begin{cases} w_0 = \sum\limits_{i=0}^{t} \\ w_1 = \sum\limits_{i=t+1}^{L-1} p_i = 1 - w_0 \end{cases} \tag{19}$$

Through the above Equation, the gray mean value of the whole image and the gray mean value of the two parts after division can be calculated:

$$\begin{cases} \mu = \sum\nolimits_{i=0}^{L-1} i * p_i \\ \mu_0 = \sum\nolimits_{i=0}^{t} i * p_i / w_0 \\ \mu_1 = \sum\nolimits_{L-1}^{i=t+1} i * p_i / w_1 \end{cases} \tag{20}$$

By continuously adjusting the gray value of increasing or decreasing the threshold t to repeatedly calculate σ_t^2 to maximize the inter-class variance, the best threshold for segmentation can be determined, that is, the background and the lung parenchyma can be best separated.

Segmentation of regional growing lung parenchyma based on OTSU

The image used in the algorithm in this paper is a 16-bit DICOM format lung medical image. The specific algorithm steps are as follows: Read the original image in DICOM format: The OTSU algorithm to first perform binarization pre-segmentation is used on the left lung parenchyma. After obtaining the pre-segmented lung parenchyma, mask processing is performed using the region growing method. After the mask processing result is obtained, the holes with an area smaller than T in the result image are filled. Holes in larger areas are processed as connected areas. After the connected area is obtained, morphological opening operation, erosion operation and smoothing are performed. After the above processing, the outline of the lung parenchyma segmented on the left can be obtained first, and the same operation processing can be performed to segment the right lung parenchyma. Finally, after the segmentation is completed, the left and right lung parenchyma are merged and fused to obtain a complete lung parenchyma result, which is then denoised [20]. The experimental results are shown in Fig. 6:

In this section, the preprocessed and segmented lung parenchyma can be reconstructed by using more reliable volume rendering and surface rendering algorithms. And the azimuth observation is realized through the 3D rotation effect, which is convenient for medical workers to diagnose the details, and has a good auxiliary effect.

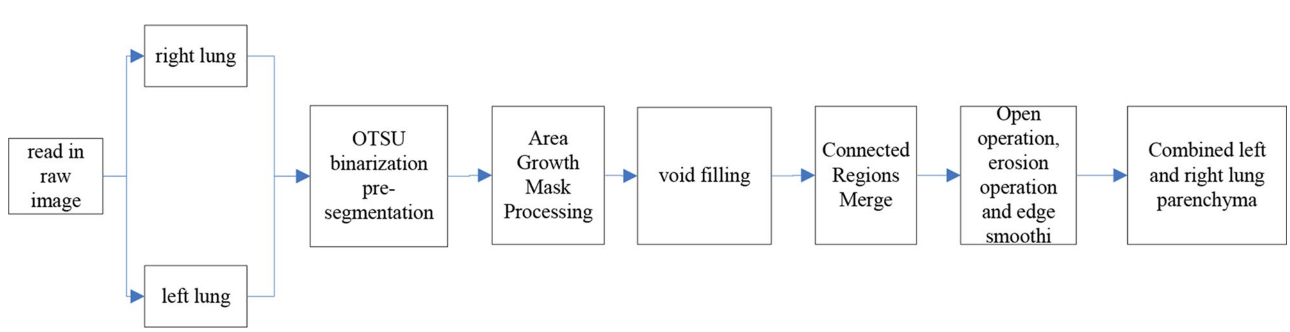

Fig. 5 Algorithm flowchart

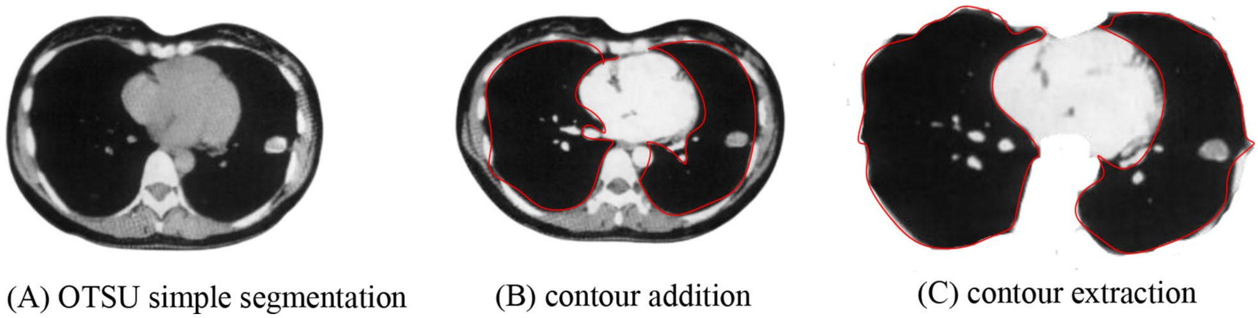

Fig. 6 OTSU lung parenchyma segmentation result

Table 1 CT parameter settings and radiation agent descriptive data

Sequence	Tube voltage (kVp)	Tube current (mAs)	CTDIvol(mGy)	DLP(mGy.cm)	E (mSv)
1	80	100	6.96	245	3.45
2	80	200	8.78	369	4.65
3	100	300	6.11	245	3.85
4	80	120	5.45	175	2.96
5	120	120	4.63	86	2.32
6	100	100	2.53	143	1.74
7	120	40	1.25	69	0.85
8	100	20	1.55	78	0.56
9	120	60	1.95	63	0.50
10	100	10	0.42	84	0.32
11	80	20	0.31	21	0.25
12	100	10	0.28	9	0.36

Table 2 Descriptive data and comparison of sensitivity, FP, FN and RVE of the four AIADS

system	Sensitivity (%) Median (P25,P75)	FP Median (P25, P75)	FN Median (P25, P75)
A	62(53.33,60)	135(5.17.5)	7(6.7)
B	100(100,100)	1(0,25)	0(0, 0)
C	76.34(73.33,73.3)	7(3, 14)	3(4,4)
D	84.67 (80,86.67)	2(0, 1)	5(2, 3)
Comparison between groups	AdSig	AdSig	AdSig
AvsB	<0.0001*	<0.0001	<0.0001*
AvsC	<0.0001*	0.596	<0.0001*
AvsD	<0.0001*	<0.0001	<0.0001*
BvsC	<0.0001*	<0.0001 +	<0.0001*
BvsD	0.0001	0.999	<0.0001*
CvsD	0.071	<0.0001 +	0.071

Detection performance evaluation of AI pulmonary nodule auxiliary diagnosis system

The density and size of pulmonary nodules are closely related to their benign and malignant properties. Less than 1% of nodules less than 5 mm in diameter are malignant. In contrast, 6% to 28% of nodules 5 to 10 mm in diameter were malignant. In contrast, nodules larger than 20 mm in diameter have a 64% to 82% chance of being malignant. Studies have shown that GGNs are more likely to be malignant than solid nodules. Due to the relatively small size of nodules less than 5 mm in diameter and the low density of GGNs, it has been difficult to qualitatively assess them in the past. However, with the development of CT technology, the detection rate of pulmonary nodules has also increased. Therefore, the research in this part analyzes the performance of different AIADS software in measuring and detecting different types of pulmonary nodules, and finds the deficiencies of the AI system, thereby providing information that can contribute to the improvement of AIADS algorithms and techniques.

CT scan image data acquisition

Phantoms with 15 simulated lung nodules were scanned using SIEMENS SOMATOM Definition Flash CT, as shown in Table 1:

The above 12 sets of parameter images are respectively reconstructed using different convolution kernels in the filtered back-projection algorithm. In order to meet the needs of the AI system to recognize images, the reconstructed layer thickness and layer spacing are both 1 mm, and other parameters remain unchanged. Finally, the 36 sets of reconstructed images are transferred to the image storage and transmission system.

Comparison of overall performance of AIADS

The sensitivity, FP, FN and RVE results of the four AIADS and the comparison between groups are shown in Table 2.

It can be seen from the table that the median sensitivity of system B is the highest, up to 100%, while the median sensitivity of system A is the lowest (60%).

Influence of parameter setting on each software

(1) Sensitivity

The average sensitivity of each AIADS under different CT dose and convolution kernel conditions is shown in Fig. 7.

As can be seen from the data presented in Fig. 7, for systems A, B, and C, there was no statistical difference in sensitivity between groups at different effective doses and convolution kernel conditions ($P > 0.05$).

(2) False positives and false negatives

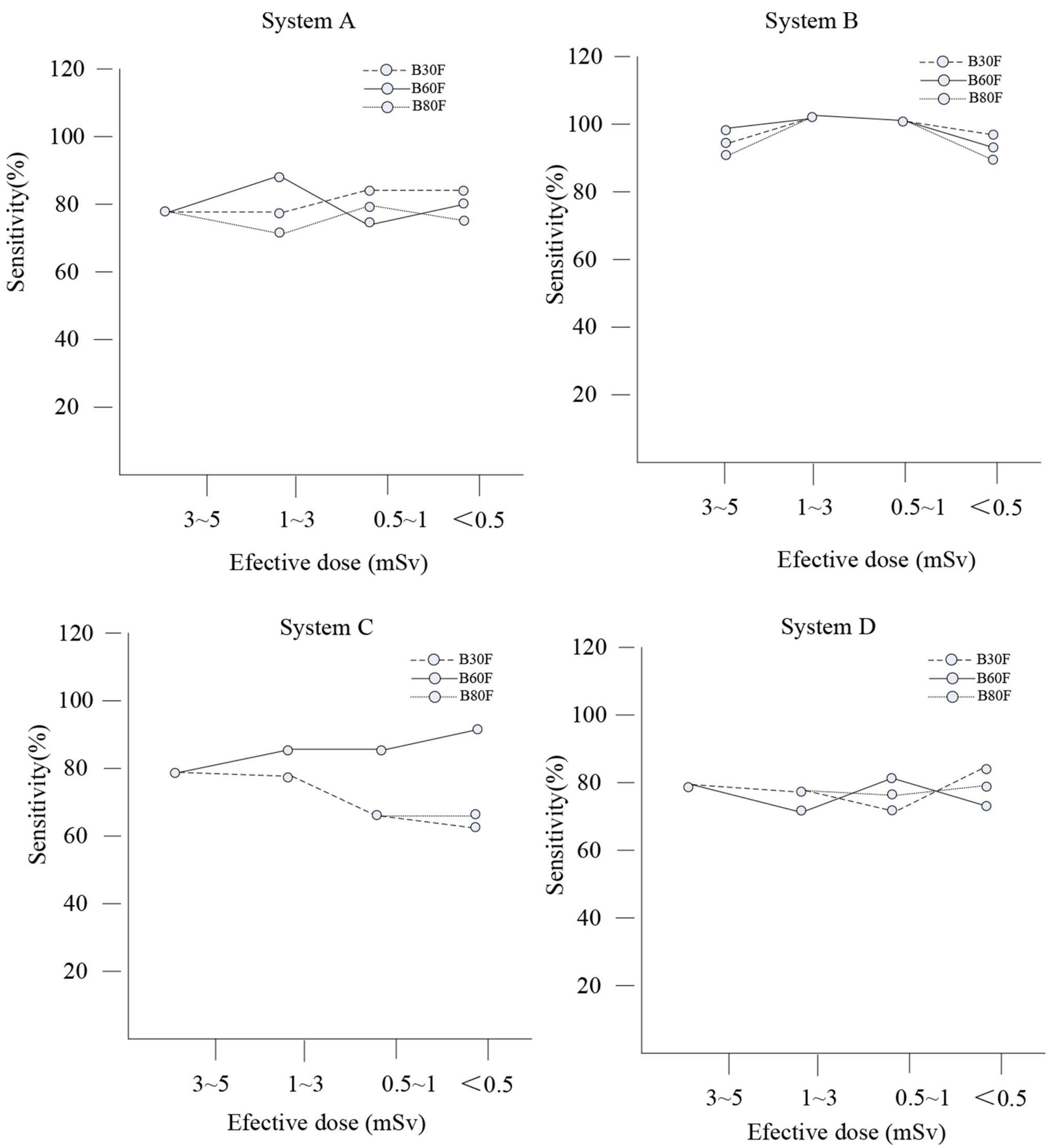

Fig. 7 Statistics of the average sensitivity of each AIADS under different CT doses and convolution kernels

False positive refers to the test result being incorrectly displayed as positive, when there is actually no disease or lesion; false negative refers to the test result being incorrectly displayed as negative, when there is actually a disease or lesion. Both errors will affect the accuracy of diagnosis. False positives may lead to unnecessary treatment and examinations, while false negatives may miss the early detection of the disease and delay treatment. Therefore, in medical testing, reducing false positives and false negatives is an important goal to improve diagnostic reliability. This article tests False Positive and False Negative, and the results are shown in Fig. 8.

As can be seen from Fig. 8, for system A, when the convolution kernels are B60f and B80f, and E decreases to the lowest, its FPs increase to 35.67 and 39.33 (PI = 0.001), respectively. For System C, FP and FN were not significantly different between the dose groups (P > 0.05); however, the FPs of the B30f group were higher than that of the B80f group (P2 < 0.0001) under all dose conditions.

Performance evaluation of ai-assisted detection software in identifying and measuring four types of pulmonary nodules

The research in this part analyzes the performance of different AIADS software in measuring and detecting different types of pulmonary nodules, and finds the deficiencies of the AI system, thereby providing information that can contribute to the improvement of AIADS algorithms and techniques. According to the density and diameter of simulated lung nodules, they were divided into: small ground glass nodules with a diameter of 5.33 ± 2.18 mm and a density of – 800 HU or – 630 HU. Small solid nodules were 5.33 ± 2.18 mm in diameter and + 100 HU in density. GGN (diameter 11 ± 1.1 mm, density – 800 HU or – 630 HU) and SN (diameter 11 ± 1.1 mm, density + 100HU). A partial CT image obtained by scanning the phantom is shown in Fig. 9, showing four types of lung nodules in different scan layers.

The MDR (Missed Detection Rate) of the four AIADS for different types of pulmonary nodules are shown in Table 3. All four systems correctly identified the SN. Among them, system B has the smallest MDR in identifying various types of nodules, the MDR for SGGN is 4.17%, and the MDR for other types of nodules is 0. In terms of identifying SGGN, there were statistical differences in the MDR comparison of each system, and the MDR size was B < D < C < A. For SSN, except for systems A and D, the MDR of each system was significantly different, respectively, B < C < A < D. For GGN, the MDR of system A (47.22%) was significantly higher than that of other systems.

ROC curve analysis showed that there was a “one vs all” relationship among the four types of pulmonary nodules, namely SGGN/other types of nodules, SSN/other types of nodules, GGN/other types of nodules, and SN/other types of nodules. Overall, systems B, C, and D had better diagnostic performance for nodules other than SSN, and all AUCs were > 0.80. System A performed poorly in classifying SGGN, SSN, and GGN (AUCs of 0.79, 0.57, and 0.56, respectively), as shown in Fig. 10.

As can be seen from Fig. 10, in the classification of pulmonary nodules, this paper analyzes the ability of AIADS to identify four types of nodules. System B had a significantly lower MDR than the other systems and was more sensitive in identifying small and hypodense nodules. All systems performed well in identifying SNs, probably due to their larger diameter and higher density. In contrast, SGGN is more difficult to identify. Because of its relatively low density, small diameter, and poorly defined boundaries, software has difficulty identifying small ground-glass nodules. In addition, it has been found significant differences between the detection performance of each AIADS. Although a certain system has the best performance in certain aspects, such as the accuracy of measuring nodule volume (such as, System D) or the accuracy of identifying nodule type (such as, System B). But no pulmonary nodule assessment system consistently outperforms others in every respect.

Conclusions

This paper mainly expounds the entire framework design requirements and steps of the medical diagnosis assistance system based on AI, and uses three improved segmentation algorithms to achieve high-precision segmentation of lung parenchyma. Another algorithm is to strengthen the edge contour of the lung parenchyma by enhancing the preprocessing and filtering operations, and then manually draw points for segmentation, which also achieves good results. In summary, the application of AI in the medical field has shown its advantages, and it has achieved remarkable achievements in the high detection rate of pulmonary nodules and the differential diagnosis of benign and malignant pulmonary nodules. The application of AI in the field of medical imaging can not only liberate the labor of radiologists, but also assist doctors in identifying benign and malignant nodules. Although there are some limitations of AI at present, it is generally considerable, especially for grass-roots hospitals that lack doctors with high professional titles and high-end equipment. AI can enable grass-roots hospitals that lack high-level doctors and high-end equipment to quickly obtain higher diagnostic capabilities and levels, thereby making the medical level more uniform. Equitable access to reliable and affordable computer-aided diagnosis for early cancer diagnosis promises to eliminate inequalities in morbidity and mortality across populations. With the continuous optimization of AI technology, it will definitely enhance the ability of radiologists

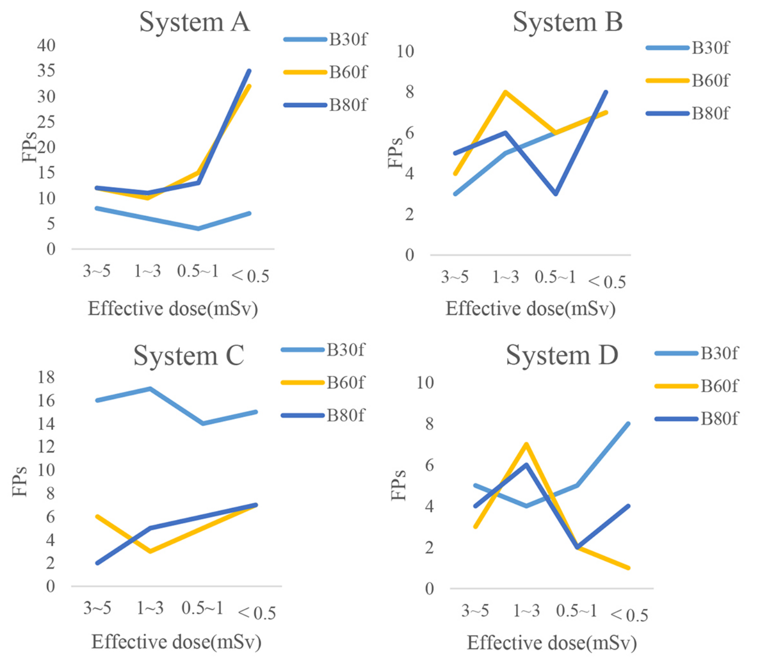

(A) The number of false positives under different convolution kernels and effective doses of each software

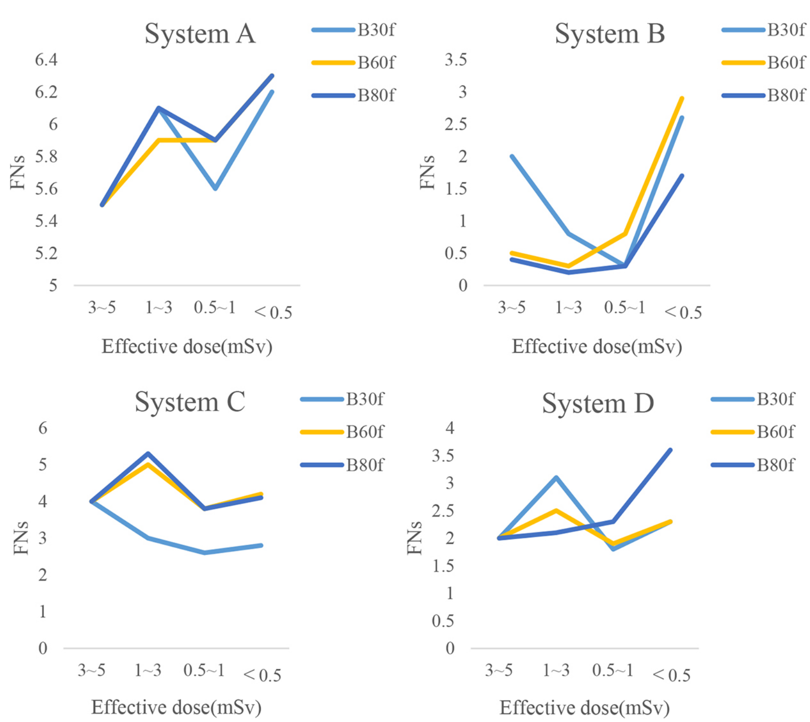

(B) False negatives under different convolution kernels and effective doses of each software

Fig. 8 Number of false positives and false negatives

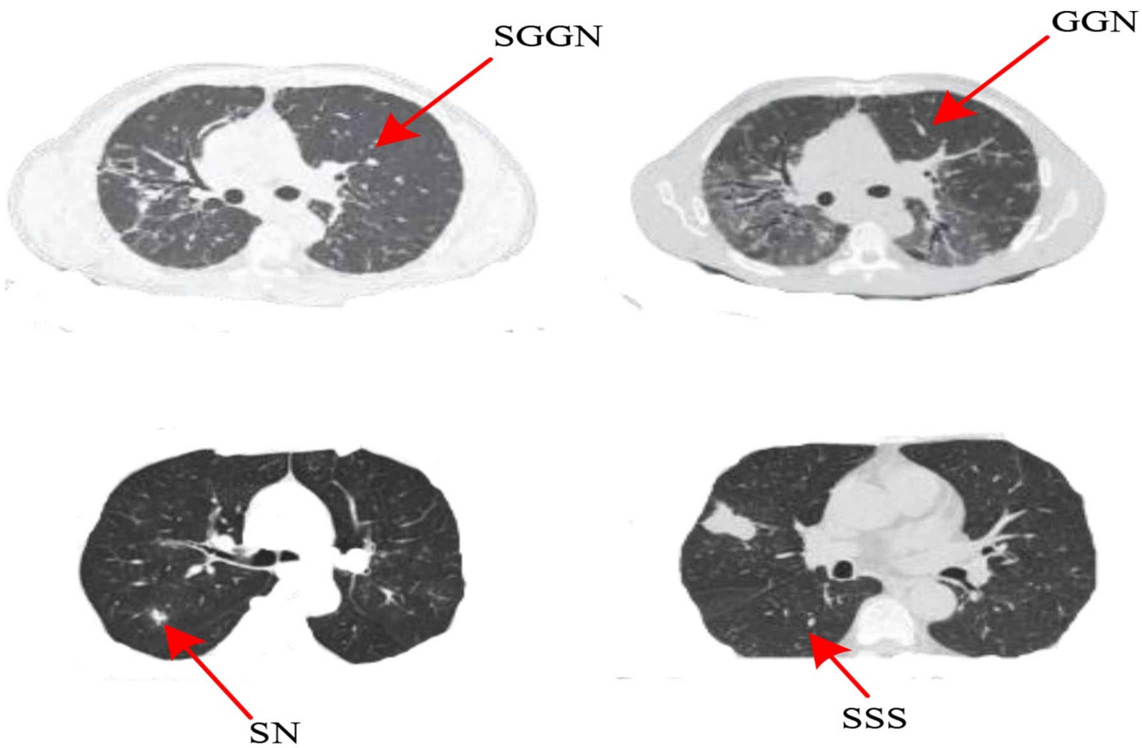

Fig. 9 Different types of simulated lung nodules CT images in the phantom

Table 3 MDR of the four AIADS for different types of pulmonary nodules

System	**MDR (100%)**			
	SGGN	**SSN**	**GGN**	**SN**
A	77.3	56.93	50.22	0
B	5.16	0	0	0
C	65.32	10.56	16.17	0
D	20.98	45.33	0.69	0
Comparison between groups	Statistics	Statistics	Statistics	Statistics
AvsB	211.30	85.17	91.02	-
AvsC	5.62	76.9	75.91	-
AvsD	87	1.35	65.56	-
BvsC	145.3	Fisher	Fisher	-
BvsD	46	44.8	Fisher	-
CvsD	85.7	28.61	Fisher	-

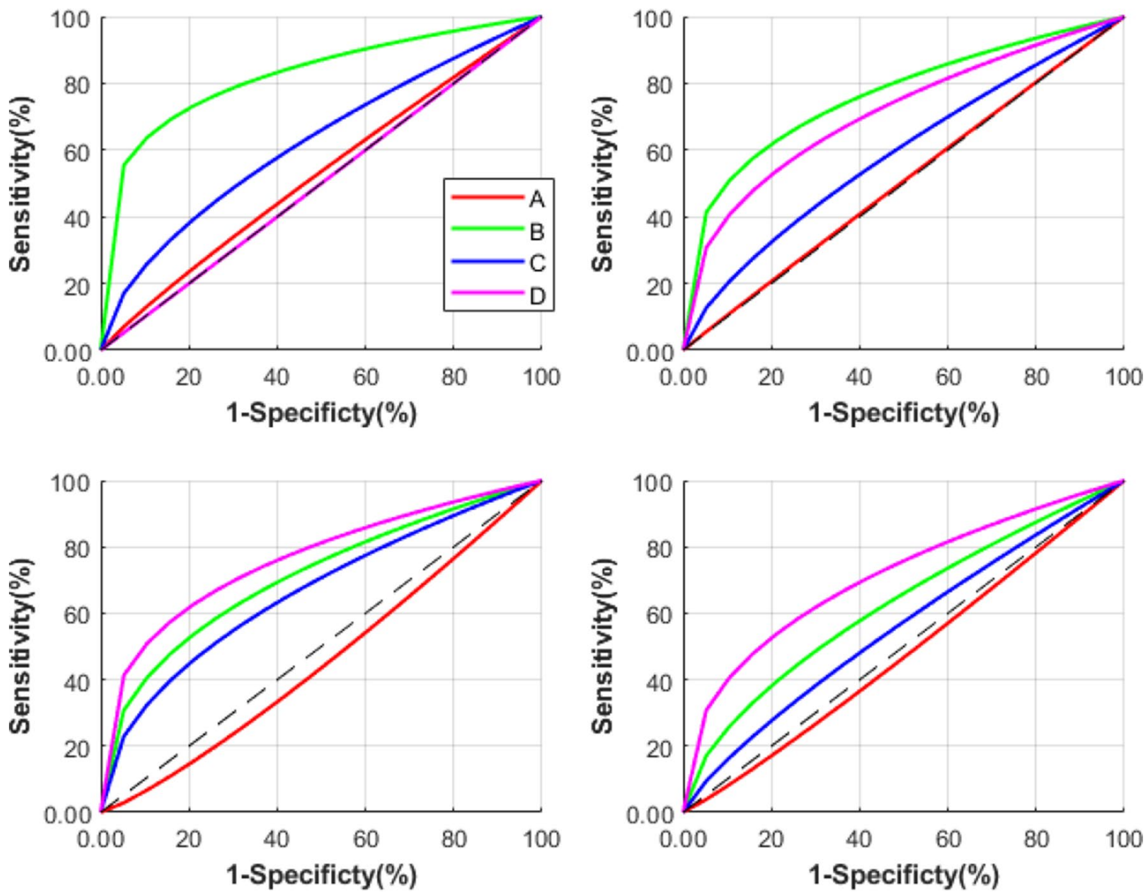

Fig. 10 One-to-many ROC curve

to detect and diagnose early-stage lung cancer, further reduce the mortality rate of lung cancer, and bring about progress in treatment methods.

Abbreviations

3D	Three-Dimensional
AI	Artificial Intelligence
AIADS	AI-Assisted Detection Software
AUC	Area Under the Curve
CAD	Computer-Aided Diagnosis
CNN	Convolutional Neural Network
CT	Computed Tomography
CTDIvol	CT Dose Index Volume
DenseNet	Dense Convolutional Network
DICOM	Digital Imaging and Communications in Medicine
DLP	Dose-Length Product
FN	False Negative
FP	False Positive
GGN	Ground-Glass Nodule
HU	Hounsfield Unit
IgH	Immunoglobulin Heavy Chain
MALT	Mucosa-Associated Lymphoid Tissue
MDR	Missed Detection Rate
MOS	Mean Opinion Score
MRI	Magnetic Resonance Imaging
OTSU	Otsu's Thresholding Algorithm
P25, P75	25th and 75th Percentiles
Paramiko	Python library for SSH protocol implementation
PET	Positron Emission Tomography
ResNet	Residual Network
RMS	Root Mean Square
ROC	Receiver Operating Characteristic
RVE	Relative Volume Error
SFTP	Secure File Transfer Protocol
SGGN	Small Ground-Glass Nodule
SN	Solid Nodule
SPN	Solitary Pulmonary Nodule
SSH	Secure Shell
SSN	Small Solid Nodule
TCP	Transmission Control Protocol
VTK	Visualization Toolkit

Acknowledgements

Not applicable.

Author contributions

Ya Yang, Pan Wang and Jinping Sheng wrote the main manuscript text, Chengzhou Yu and Jing Zhu prepared Figures 1-10. All authors reviewed the manuscript.

Funding

This study was supported by the Research and Development Program of The General Hospital of Western Theater Command(Grant No. 2024-YGJS-B01 and 2024-YGJS-A05).

Data availability

The data that support the findings of this study are available from the corresponding author upon reasonable request.

Declarations

Ethics approval and consent to participate
The study was approved by the Ethics Committee of the Chinese People's Liberation Army Western Theater Command General Hospital. Informed consent has been obtained from all participants, 2024ky203-1. Declaration of Helsinki - My research complies with the Helsinki Declaration.

Consent to participate
Informed consent was obtained from each participant.

Consent for publication
Not applicable.

Competing interests
The authors declare no competing interests.

Received: 22 October 2024 / Accepted: 21 April 2025
Published online: 14 May 2025

References
1. Zheng G, Han G, Soomro NQ.An Inception Module CNN Classifiers Fusion Method on Pulmonary Nodule Diagnosis by Signs[J]. Tsinghua Sci Technol. 2020;25(3):368–83.
2. Zhang S, Sun F, Wang N, Zhang C, Yu Q, Zhang M, et al. Computer-Aided Diagnosis (CAD) of Pulmonary Nodule of Thoracic CT Image Using Transfer Learning[J]. J Digit Imaging 2019;32:995–1007.
3. Zhang N, E L, Wu S, Wu Z.CT texture analysis in differential diagnosis of benign and malignant solitary pulmonary nodule[J]. Chin J Med Imaging Technol. 2018;34(8):1211–15.
4. Vayntrub Y, Gartman E, Nici L, Jankowich MD.Diagnostic Performance of the Herder Model in Veterans Undergoing PET Scans for Pulmonary Nodule Evaluation[J]. Lung. 2021;199(6):653–57.
5. Wang Y, Wu B, Zhang N, Liu J, Zhao L.Research progress of computer aided diagnosis system for pulmonary nodules in CT images[J]. J X-Ray Sci Technol. 2019;28(1):1–16.
6. Singh S, Karimi S, Ho-Shon K, Show HL.Tell and summarise: learning to generate and summarise radiology findings from medical images[J]. Neural Comput Appl. 2021;33(13):7441–65.
7. Ha W, Vahedi Z.Automatic Breast Tumor Diagnosis in MRI Based on a Hybrid CNN and Feature-Based Method Using Improved Deer Hunting Optimization Algorithm[J]. Comput Intell Neurosci. 2021;2021(3):1–11.
8. Saygili A, Albayrak S.An efficient and fast computer-aided method for fully automated diagnosis of meniscal tears from magnetic resonance images[J]. AI Med. 2019;97(JUN.):118–30.
9. Barinov L, Jairaj A, Becker M, Seymour S, Lee E, Schram A.Impact of Data Presentation on Physician Performance Utilizing AI-Based Computer-Aided Diagnosis and Decision Support Systems[J]. J Digit Imaging. 2019;32(3):408–16.
10. Loku L, Fetaji B, Krsteski A.Automated medical data analyses of diseases using big data[J]. Knowl Int J. 2018;28(5):1719–24.
11. Nasrallah NA, Sears CR.Biomarkers in Pulmonary Nodule Diagnosis: is It Time to Put Away the Biopsy Needle?[J]. Chest. 2018;154(3):467–68.
12. Shimomura M, Ishihara S.A case of pulmonary MALT lymphoma with preoperative definitive diagnosis based on IgH rearrangement in paraffin-embeded specimen[J]. J Jpn Ass Chest Surg. 2017;31(2):221–26.
13. Havinga P, Meratnia N, Bahrepour M.AI based event detection in wireless sensor networks[J]. Univ Twente. 2017;85(6):1553–62.
14. Glauner P, Meira JA, Valtchev P, State R, Bettinger F.The Challenge of Non-Technical Loss Detection using AI: a Survey[J]. Int J Comput Intell Syst. 2017;10(1):760–75.
15. Chen AF, Zoga AC, Vaccaro ARP.Counterpoint: AI in Healthcare[J]. Healthc Transform. 2017;2(2):84–92.
16. Hutson M.AI faces reproducibility crisis[J]. Science. 2018;359(6377):725–26.
17. Lemley J, Bazrafkan S, Corcoran P.Deep learning for consumer devices and services: pushing the limits for machine learning, AI, and computer vision[J]. IEEE Consum Electron Mag. 2017;6(2):48–56.
18. Price S, Flach PA.Computational support for academic peer review: a perspective from AI[J]. Commun ACM. 2017;60(3):70–79.
19. Agrawal A, Gans JS, Goldfarb A.What to expect from AI[J]. MIT Sloan Manage Rev. 2017;58(3):23–26.
20. Labovitz DL, Shafner L, Gil MR, Hanina A.Using AI to Reduce the Risk of Nonadherence in Patients on Anticoagulation Therapy[J]. Stroke. 2017;48(5):1416–19.

Publisher's Note